RSC Advances

ROYAL SOCIETY OF CHEMISTRY

www.rsc.org/advances

RSC Advances

ARTICLE

Multifunctional Au nanoclusters for targeted bioimaging and enhanced photodynamic inactivation of *Staphylococcus aureus*

Received 00th January 20xx,
Accepted 00th January 20xx

DOI: 10.1039/x0xx00000x

www.rsc.org/

Boris Khlebtsov,[a,b] Elena Tuchina,[b] Valery Tuchin,[b,c,d] and Nikolai Khlebtsov[a,b,*]

Fluorescent Au nanoclusters (NCs) have been the subject of intense studies owing to their increasing applications in imaging, sensing, and nanomedicine. Herein, highly fluorescent bovine serum albumin (BSA)-directed Au–BSA NCs are synthesized as a platform for further conjugation with human antistaphylococcal immunoglobulin (antiSAIgG) and the photodynamic (PD) synthesizer Photosens™ (PS) to fabricate Au–BSA–antiSAIgG–PS complexes. The complexes possess three theranostic modalities: biospecific detection of *Staphylococcus aureus* bacteria, intense red fluorescence due to Au–BSA NCs (quantum yield, ~14%), and synergistic PD inactivation due to the PS dye. Owing to biospecific targeting and intense red fluorescence, the Au–BSA–antiSAIgG probe can detect pathogenic bacteria in bacterial mixtures through fluorescence microscopy or even through naked eye inspection of sediments under UV illumination. The developed complexes can be used at physiological pH of ~7, in contrast to nonspecific electrostatic binding of Au–human serum albumin NCs to *S. aureus* at pH <5–6. PD treatment of methicillin-sensitive and methicillin-resistant *S. aureus* with Au–BSA–antiSAIgG–PS complexes and 660 nm light irradiation significantly inactivates both types of bacteria. By using the developed strategy, Au–BSA–PS complexes can be further modified with other targeting and chemotherapeutic molecules, thus ensuring new theranostic applications in current nanomedicine.

1. Introduction

Noble metal nanoclusters (NCs) are a new type of fluorophores[1-3] that have attracted significant attention owing to their advantageous photophysical properties, as compared to small-molecule dyes, fluorescent proteins, quantum dots, and upconverting and dye-doped nanoparticles.[4-7] Today, highly fluorescent stable NCs can be fabricated with atomically precise sizes and tunable optical properties.[8-11] For biomedical applications, Au NCs have been synthesized by using biocompatible capping ligands, including DNA,[12,13] glutathione (GSH),[14,15] bovine serum albumin (BSA),[16] and other proteins (see, e.g., Refs.[17,18] and references therein). Moreover, $HAuCl_4$ can serve as a precursor without any reducing agent to obtain fluorescent Au NCs under native conditions through *in vivo* biosynthesis.[19,20] Protein-based protocols hold particular promise, as proteins act as reducing and stabilizing agents that produce water-soluble, biocompatible, and low-toxic[21] NCs under mild reaction conditions.[12] Protein-capped NCs retain their fluorescence (FL) in a wide range of pH and can easily be conjugated with target and drug molecules. Most published applications of Au NCs have been focused on sensing, bioimaging *in vitro* and *in vivo*,[4,19,22-25] and catalysis.[6,26,27]

The excessive use of antibiotics in human and animal medicine has led to the emergence of multidrug-resistant (MDR) bacterial infections. In the past few decades, several pathogens have acquired MDR to various antibiotics. Methicillin-resistant Staphylococcus aureus (MRSA)[28] is a serious problem for many clinics, as it is responsible for a wide range of diseases, including skin and soft tissue infections, life-threatening pneumonia and sepsis, septic arthritis, endocarditis, toxic shock syndrome, and osteomyelitis.[29-31]

The main challenge in treating MRD pathogens comes from the continual emergence of new MRD strains with a parallel significant decline in new market-available antibiotics.[31,32] This situation clearly points to the urgent need to develop new, nonantibiotic strategies for curing MRD infections. Another challenge is associated with the sensitive, early detection of MRD pathogens, as the standard culturing methods are time-consuming, tedious, and impractical for real-time applications.[32]

Both challenges can be resolved with the use of multifunctional theranostic nanocomposites that combine therapeutic, diagnostic, and sensing modalities in a single nanostructure.[33-37] In this regard, protein- or glutathione-

[a] *Institute of Biochemistry and Physiology of Plants and Microorganisms, Russian Academy of Sciences, 13 Prospekt Entuziastov, Saratov 410049, Russia.*
[b] *Chernyshevsky Saratov State University, 83 Ulitsa Astrakhanskaya, Saratov 410012, Russia.*
[c] *Institute of Precise Mechanics and Control, Russian Academy of Sciences, 24 Ulitsa Rabochaya, Saratov 410028, Russia.*
[d] *Tomsk State University, 36 Prospekt Lenina, Tomsk 634050, Russia.*
* E-mail: khlebtsov@ibppm.sgu.ru

Electronic Supplementary Information (ESI) available: Synthesis and additional characterization of Au–BSA and Au–HSA NCs, evaluation of Au–BSA cluster size, evaluation of the QY for Au–BSA NCs, dot immunoassay of Au–BSA–IgG NCs, calibration plot for determination of the PS concentration from the absorbance at 675 nm, absorbance spectra of PS, NCs, and complexes in the spectral band 230-400 nm, binding of Au–BSA and Au–HSA NCs to bacteria at pH 4 and 6. See DOI: 10.1039/x0xx00000x

capped Au NCs seem more promising as nanoplatforms than larger-sized plasmonic nanoparticles. Indeed, owing to the strong intrinsic FL of Au NCs, there is no need to functionalize them with FL dyes for diagnostic purposes. What is more, owing to their small sizes, Au NCs can be metabolized by renal clearance, thus decreasing potential nanotoxicity[21] (see, however, the recent report by Dong et al.[38]). By contrast, all organs of the reticuloendothelial system are the primary targets of accumulating Au nanoparticles with sizes ranging from 5 to 100 nm.[39] As the excretion of accumulated particles from the liver and spleen can take up to 3 to 4 months, the question as to the possible inflammation processes is of great importance.

Thus, the development of multifunctional NC platforms for theranostic applications seems very desirable. However, in contrast to the numerous studies on multifunctional composites based on plasmonic nanoparticles,[40,41] there have been few reports describing analogous NC-based multifunctional theranostic nanocomposites. Furthermore, those studies were aimed mainly at cancer theranostics. One of the first investigations dealing with multifunctional NCs was conducted by Retnakumar et al.,[42] who prepared BSA-protected Au NCs conjugated with folic acid (Au–BSA–FA) for receptor-targeted detection of oral squamous cell carcinoma (KB) and breast adenocarcinoma MCF-7 cells. Similarly, Wang et al.[43] synthesized BSA-protected Au NCs, which were conjugated with herceptin (Au–BSA–Her) to achieve specific targeting and nuclear localization in the overexpressed ErbB2 receptors. Perhaps the first reports on the theranostic application of Au NCs were published by Chen *et al.*[44,45], in which Au–BSA NCs were additionally loaded with FA, methionine (MET), doxorubicin (DOX), or the near-infrared (NIR) fluorescent dye MPA. Ding and Tian[46] applied Au–BSA–FITC–FA NCs to specific bioimaging and biosensing of cancer cells, in which Au NCs produced a reference FL signal, FITC allowed the monitoring of the pH, and FA acted as targeting molecules. Finally, Cui and coworkers[47] recently developed multifunctional theranostic NCs comprising GSH-capped Au NCs; after these were further coupled to FA and PEG, the photosensitizer chlorin e6 (Ce6) was trapped within PEG networks. To summarize, there is an evident lack of studies focused on the development of Au NCs for antimicrobial theranostics.

In recent years, few plasmonic nanocomposites have been developed for simultaneous detection and PD and photothermal inactivation of bacterial pathogens (see Refs.[29,48-50] and references therein). Chen et al.[51] demonstrated that lysozyme-based Au NCs serve as potential antimicrobial agents for antibiotic-resistant bacteria. Chan and Chen[52] used human serum albumin (HSA) as a capping agent to synthesize Au–HSA NCs. These NCs were used as sensing probes for several pathogenic bacteria, and a selective sensing ability toward *S. aureus* and MRSA was observed. In this work, we found, however, that the selective binding of Au–HSA NCs to methicillin-sensitive *S. aureus* (MSSA) and MRSA is strongly pH dependent and that a nonspecific interaction can be observed at very small variations in pH. Furthermore, the Au–HSA NCs[52] did not include any inactivation agents or related antimicrobial activity. It should also be emphasized that targeting at acidic pH<5–6 cannot be used for *in vivo* applications, e.g., for the early detection of pathogenic bacteria in the bloodstream.[32]

Thus, to the best of our knowledge, there have been no reports on the application of multifunctional fluorescent Au NCs to selective detection and PD inactivation of pathogenic bacteria. Here, we describe Au–BSA NCs functionalized with targeting molecules (human antistaphylococcal immunoglobulin, antiSAIgG) and the PD dye Photosens™ (PS)[53] for selective detection and effective PD inactivation of both MSSA and MRSA. For brevity, antiSAIgG will further be designated simply as IgG. The resultant multifunctional NCs (complexes) will be designated Au–BSA–IgG–PS.

2. Results and Discussion

2.1. Synthesis and Characterization of Au–BSA NCs and Multifunctional Complexes

2.1.1. Synthesis of Au–BSA NCs and Au–BS–IgG–PS Complexes

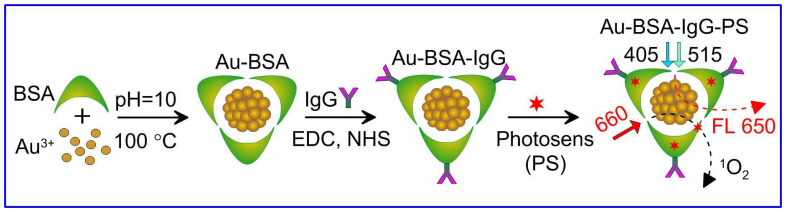

Figure 1. Scheme for the preparation of Au–BSA–IgG–PS complexes and their fluorescent and PD properties under (405, 515 nm) and 660 nm excitation, respectively. Note that 405 and 515 nm correspond to the excitation spectrum maxima. In fact, the FL excitation band lies between 350 and 600 nm (see below).

Au–BSA–IgG–PS multifunctional complexes were synthesized in three basic steps, represented schematically in **Figure 1**. First, Au–BSA NCs were prepared from a mixture of BSA and Au_3^+ under highly basic conditions and boiling temperature[16] (see Experimental Section). During the synthesis of NCs, $Au3^+$ ions are mainly reduced by the 21 tyrosine residues in BSA through the phenolic groups.[16,54] According to previous studies,[16,54,55] Au–BSA

NCs are made up of 20[54] or 25[16,55] gold atoms and are stabilized by the thiol group of cysteine in BSA. Such Au–BSA NCs have been proposed to have a core–shell structure in which Au(0) atoms form an icosahedral core surrounded by –S–Au(I)–S–Au(I)–S– staples.[55] With account taken of the reagent concentrations in the synthetic protocol used, the number of Au atoms per BSA molecule in our Au–BSA cluster was 20 (ESI file, Section S1).

2.1.2. Characterization of Au–BSA NCs and Au–BS–IgG–PS Complexes

Figure 2 shows the extinction (1), excitation (2), and emission spectra of Au–BSA NCs and emission spectrum of BSA (4). The FL excitation spectrum (curve 2 in Fig. 2a) exhibits two maxima around 405 and 514 nm. The emission peaks are located near 470 and 660 nm. From a comparison with the BSA emission spectrum (4), we attribute the first peak to the FL of BSA alone, whereas the second peak originates from NC luminescence HOMO–LUMO electronic transitions, as reported earlier.[16] In general, the extinction spectrum is close to that for small (<3 nm) Au nanoparticles,[56] which have no plasmonic peak around 510–520 nm. Therefore, absorption spectrum (1) indicates the formation only of a pure NC solution, without larger or aggregated Au nanoparticles. As shown in the inset of Fig. 2b, the as-prepared Au–BSA NCs were highly dispersed in aqueous solution and exhibited a brown color under white light and strong red FL under UV illumination. Additional images under illumination at 405 nm and 520 nm are shown in **Figure S1** (ESI).

TEM images of NCs (Fig. 2b) also confirm the absence of large or aggregated nanoparticles. Note that the TEM images also show that all Au NCs were associated with BSA (gray areas). Additional representative TEM images of Au–BSA NCs and a size-distribution histogram are shown in **Figure S2** (ESI). The average NC size, derived from 100 cluster images, was determined to be $d_{av} = 1.8 \pm 0.4$ nm. For illustrative comparison, the inset in Fig. S2 c shows an HRTEM image of Au_{20}-MPA_{15} NC with the average size $d_{av} = 1.12 \pm 0.43$ nm, as estimated by Sahoo et al.[57] Although the average sizes of our Au_{25}–BSA (1.8 nm) and Au_{20}–MPA_{15} (1.1 nm) clusters differ by 60%, the TEM images look very similar at equivalent magnification. For crystalline Au, the average lattice spacing is about 0.3 nm, thus giving 220 atoms for 1.8-nm NCs. This value is almost an order of magnitude higher than the expected 25 atoms. Evidently, the average NC size that is in agreement with 25 Au atoms should be about 1 nm or a bit smaller than that. However, for highly fluorescent Au NCs capped with different agents (BSA, GSH, PAMAM, etc.), the reported TEM sizes are greater than 1 nm (ESI, Table S1). Specifically, Table S1 lists data from 10 publications on Au_{25}–BSA NCs and 4 publications on the related GSH-capped Au_{25}–SG_{18} and Au_{20}–MPA_{15} NCs (MPA designates mercaptopropionic acid). It follows from the Table S1 data that the typical TEM size of highly fluorescent Au–BSA NCs is about 2 nm. Thus, for BSA-stabilized Au NCs, the average TEM size cannot be treated as the single-crystalline parameter. For instance, Sahoo et al.[57] did not observe any distinct lattice spacing of single crystalline in their HRTEM images. The existing data on this point are somewhat controversial. In particular, Zang et al.[54] reported a crystalline fcc structure for Au_{20}–BSA NCs with a lattice spacing of 0.24 nm, but their average NC size of 2.6 nm corresponds to $(2.6/0.3)^3$=650 Au atoms, which is in evident disagreement with their MALDI–TOF estimation of 20 Au atoms in a single Au NC.

Typically, the reported TEM images show complex hybrid structures formed from Au NCs and capping polymers. Because of the low contrast and indistinct boundaries, it is difficult to make a reliable estimate of the Au–BSA NC size from both standard TEM and high-resolution HRTEM images. As a rule, the size distributions of Au–BSA clusters are rather broad except for the monodisperse GSH-coated Au_{25}–SG_{18} NCs synthesized by Jin and coworkers.[58] Those authors reported a special protocol for separating different fractions of 4-nm and 2-nm Au nanoparticles from 1-nm Au_{25}–SG_{18} NCs. However, the monodisperse Au_{25}–SG_{18} NCs demonstrated a very low quantum yield (QY) (less than 1 %), in contrast to our highly fluorescent Au–BSA NCs, with a QY of about 14%. Recently, Xei and coworkers[59] discovered a new highly fluorescent GSH-capped $Au_{22}(SG)_{18}$ NCs with a QY of about 8%, in contrast to low fluorescent NCs with similar molecular formulae—$Au_{22}(SR)_{16}$, $Au_{22}(SR)_{17}$, and $Au_{25}(SR)_{18}$. As the fluorescence of $Au_{22}(SR)_{18}$ originates from the long Au(I)-thiolate motifs on the NC surface via the aggregation-induced emission mechanism[60], one can expect a typical NC size of about 2 nm.

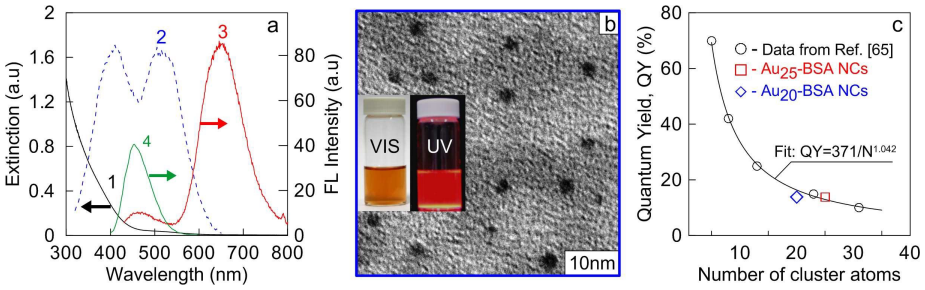

Figure 2. (a) Extinction (1), excitation (2), and emission (3) spectra of Au–BSA NCs and emission spectrum of BSA (4). (b) TEM images of Au–BSA NCs. The inset show photos of NC solutions under white light (left) and UV light (right) irradiation. (c) Dependence of the quantum yield (QY, %) on the number of cluster atoms. Black circles, data from Dickson and coworkers (Ref.[65]); red square, Au_{25}–BSA; blue rhombus, Au_{20}–BSA NCs.

Note that the spectral position of the second emission near 660 nm is close to the data of Refs. 16 and 54, whereas Wen et al.[55] observed two red emission bands, one of which was located near 710 nm (more intensive band I) and the other (less intensive band II) was located near 640 nm. Bands I and II exhibited different temperature dependences and different physical origins. The difference between the data of Wen *et al.*[55] on the one hand, and the emission spectra in Fig. 2 and the spectra reported in Refs. 16 and 54 on the other can be explained by the different structure of BSA-capped NCs.

For evaluating the QY of the Au–BSA NCs, a hematoporphyrin (HP) solution in phosphate-buffered saline (PBS) was used as a reference, as the red emission spectrum of HP is located within the red emission band of Au–BSA NCs and the QY value of HP is known from the literature.[61] For minimizing the luminescence quenching caused by internal absorption[62] (the inner filter effect),[63] the absorbance of all experimental and reference samples was adjusted to about 0.05 at the excitation wavelength (405 nm), which coincides with the absorption maximum of the reference dye. The QY can be calculated by Eq. (1), which takes into account the correction for the different refractive indexes of the sample (n) and reference (n_r) solvents and the possible difference in the extinction of the sample (E) and reference solutions (E_r)[64]

$$\phi = \phi_r \frac{\langle I \rangle n^2 (1-10^{-E_r})}{\langle I_r \rangle n_r^2 (1-10^{-E})}, \quad (1)$$

where $\langle I \rangle$ and $\langle I_r \rangle$ are the integrated emission across the luminescence band for the sample and reference solutions, respectively. As pointed out by Eaton,[62] it is most desirable that both unknown and the standard be in the same solvent. In our experiments, the sample and reference solvent was water. Further, the sample and reference extinctions were small (0.05) and almost identical. Under these conditions, Eq. (1) reduces to its simplest form, which was used for the QY calculations reported in this work

$$\phi = \phi_r \frac{\langle I \rangle}{\langle I_r \rangle}. \quad (2)$$

Under optimal conditions, the QY of our NCs was about 14 % (**Figure S3** and related comments in ESI). This value is in excellent agreement with the earlier found correlation between the NC sizes and their QYs[65] for Au_{25}–BSA NCs (Fig. 2c). Note that the measured QY value lies a bit lower than the best-fitting curve if one assumes the presence of 20 Au atoms in the Au_{20}–BSA NCs.

BSA as a capping agent contains various functional groups that are suitable for functionalization with different ligands. Specifically, BSA possesses 59 lysine amine groups, 1 free cysteine sulfhydryl, 19 tyrosine phenolate residues, and 17 histidine imidazole groups.[66] The presence of numerous carboxylate groups gives BSA its net negative charge (at pH>5). By use of the above functional groups, BSA can be modified with various target molecules and labels. For example, Au–BSA NCs were functionalized with FA[42, 54] and hyaluronic acid[54] for targeting folate-positive cancer cells. On the other hand, BSA has a fairly high sorption capacity with respect to photosensitizer dyes, drugs, and various haptens, making BSA-capped NCs a promising platform for the development of theranostic nanocomposites. To achieve this goal, in step 2, Au–BSA NCs were functionalized with human antistaphylococcal immunoglobulin (designated here simply as IgG), also known as antibodies against staphylococcal endotoxin (Fig. 1, step 2). To check the integrity of antibody functions after binding to BSA, we used two variants of dot immunoassay as described earlier.[67] In the first variant, Au–BSA–IgG complexes were conjugated to 15-nm colloidal gold (CG) nanoparticles to obtain a sensing probe for protein A on a nitrocellulose membrane (**Figure S4**, ESI). After incubation with Au–BSA–IgG–CG complexes and washing, specific binding was observed as red spots under white light illumination owing to plasmonic absorption of CG near 520 nm. In the second variant, MRSA was applied to the membrane. After incubation with Au–BSA–IgG complexes and washing, specific binding was observed as red FL spots under UV irradiation (Fig. S4b).

In the final step, Au–BSA and Au–BSA–IgG complexes were incubated in a photosensitizer PS solution (Experimental Section). As PS has a high degree of binding to serum proteins, including BSA, it was successfully included in the BSA matrix to form multifunctional Au–BSA–IgG–PS complexes. Under our experimental conditions, about 10% of the added PS was loaded after 1 h of incubation. Owing to the 100-fold difference between the molecular masses of PS and the Au–BSA–IgG–PS complexes, free PS in solution can easily be removed by using a desalting column. No desorption of PS was observed after one-week storage in PBS at pH 4 and 6. The PS loading content was evaluated by measuring the absorption at 675 nm, corrected to the absorbance of Au–BSA NCs at the same wavelength. We used a low PS:Au–BSA weight ratio to exclude the dominant PS absorption, which would make the optical features of the Au–BSA complexes indistinguishable on the strong-absorption PS background. Typically, the final loading content of PS was about 0.1 %, corresponding to 3 PS molecules per 10 Au–BSA NCs (ESI, Section 1). Cui and coworkers[47] reported a loading content of the drug

Ce6 of 6% for GSH-capped Au–GSH complexes containing NHS-activated FA-conjugated PEG (FA-PEG_{2K}–NHS). Using this loading percentage, we estimated the number of Ce6 per 10 NCs to be about 9 (ESI, Section S1). Thus, despite the difference in the average weight load being almost two orders of magnitude, the numbers of Ce6 and PS molecules per complex differ only by three times. The intermediate and final complexes were characterized by absorption and FL spectra. **Figure 3** shows the extinction spectra of a PS solution in PBS (1), Au–BSA NCs (2), the intermediate complexes Au–BSA–PS (3) and Au–BSA–IgG (4), as well as the resultant multifunctional complexes Au–BSA–IgG–Phs (5). Before measurements, all samples were normalized as follows. In all solutions, the PS concentration was kept constant and equal to 2 μg/mL, and the BSA concentration also was constant and equal to 2 mg/mL. The PS concentrations were determined by spectrophotometric calibration (**Figure S5**, ESI).

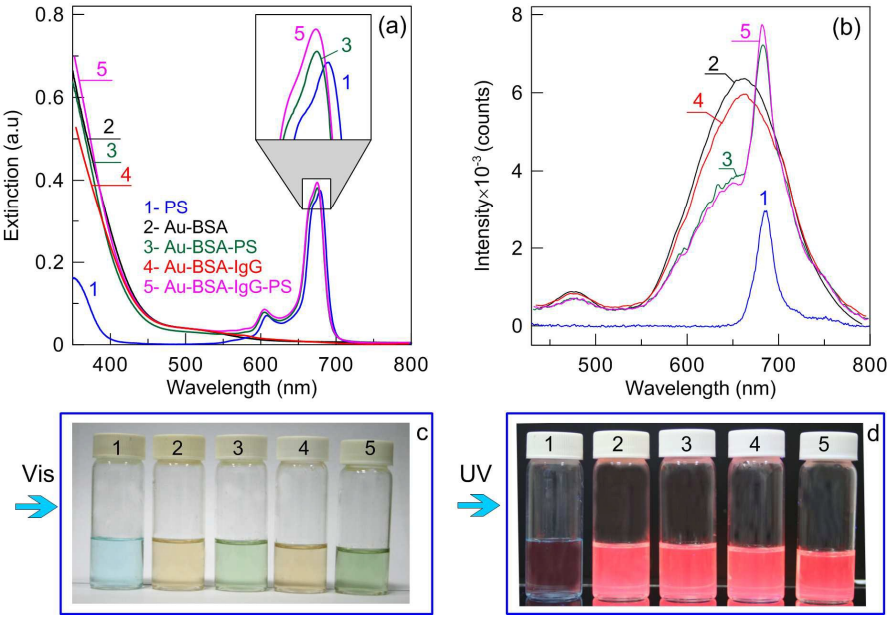

Figure 3. Extinction (a) and FL (b) spectra measured at 405 nm excitation for a PS solution (1; concentration, 2 μg/mL) in PBS, Au–BSA NCs (2), and Au–BSA–PS (3), Au–BSA–IgG (4), and Au–BSA–IgG–PS complexes (5). The inset in panel (a) illustrates weak variations in the PS emission peak for PS, Au–BSA–PS, and Au–BSA–IgG–PS. The photos in panels (c) and (d) show the color of the samples under white light (c) and UV (d) illumination. Note the intense red FL of samples 2–5 owing to Au–BSA clusters.

It is evident from Fig. 3a that all PS-containing samples exhibit adsorption peaks near 615 and 675 nm. The peak intensities are roughly constant, but the precise spectral positions are slightly different between free PS and PS-containing complexes. In general, the free PS spectrum and the spectra of PS in the BSA matrix are in agreement with previous observations.[68] Considering the UV parts of the absorption spectra (**Figure S6**, ESI), we observe weak BSA shoulders for the Au–BSA and Au–BSA–PS NCs and a more pronounced peaks of IgG near 280 nm for the Au–BSA–IgG and Au–BSA–IgG–PS NCs.

The panel (c) in Fig. 3 shows photos of all five samples under side white light illumination. The color of the samples changes from blue (1, PS) to light-brown (2, Au–BSA). Conjugation with IgG does not change the solution color (vial 4). In contrast, additional conjugation of the complexes with PS changes the solution color from blue or light-brown to light green (vials 3 and 5).

Under UV illumination (Fig. 3d), the PS solution demonstrates weak red FL, whereas all types of Au NC complexes exhibit an almost similar bright-red FL color. The FL spectra demonstrate a deep red FL peak of PS at 690 nm (Fig. 3b, curves 1, 3, and 5) under 405-nm excitation. The FL spectrum of Au–BSA NCs (curve 2) corresponds to that in Fig. 2, and conjugation with IgG does not change spectrum 2 essentially (curve 4). By contrast, additional conjugation with PS leads to the appearance of its FL peak at 690 nm and to decreased FL intensity of the Au–BSA spectral shoulder.

For assessing the PD capability of the Au–BSA and Au–BSA–IgG–PS complexes, 10-anthracenediyl-bis (methylene) dimalonic acid (ABDA) was employed as a probe molecule to monitor singlet oxygen generation. In this method, ABDA can react with the newly generated singlet oxygen to yield an endoperoxide that causes a decrease in molecule absorption at 402 nm. The photooxidation of ABDA in the presence of NCs was monitored for 60 min

under LED light irradiation at 660 nm and a power density of 50 mW/cm^2. A PS solution with a concentration of 20 ng/mL was used as a reference.

With an increase in light exposure, the characteristic absorbance peaks of ABDA, including the main peak at 402 nm, gradually decrease **(Figure 4)**.

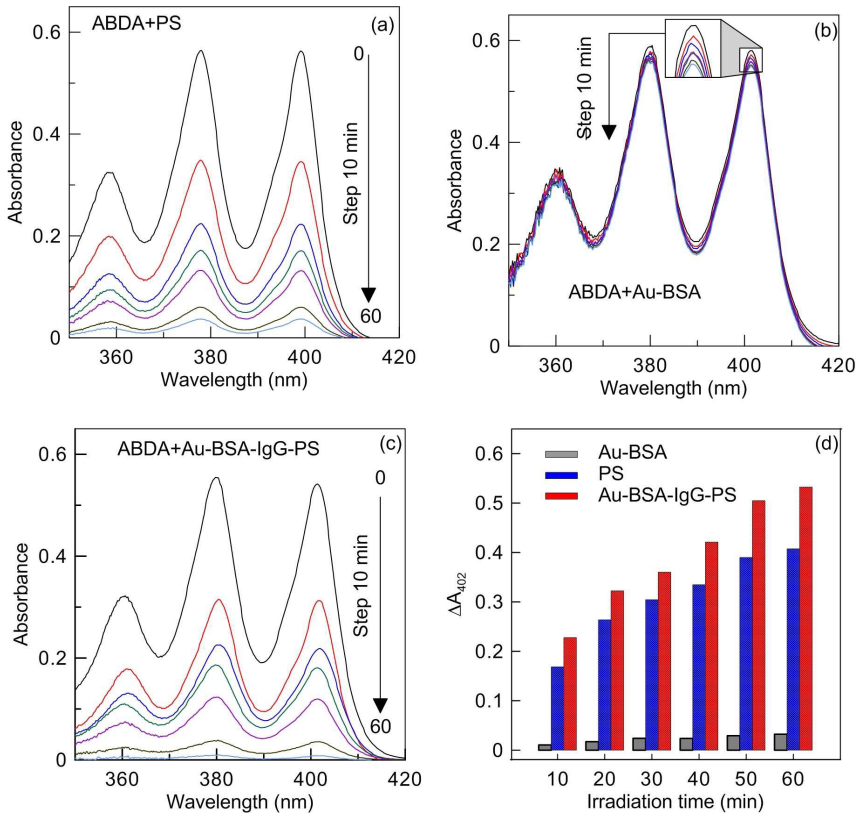

Figure 4. (a) Absorption spectra of a mixture of ABDA and PS (a), Au–BSA (b), and Au–BSA–IgG–Phs (c) under illumination by a 660-nm light source for different exposures from 0 to 60 min at a power density of 50 mW/cm^2 or a fluence of 0 to 180 J/cm^2 with a step of 30 J/cm^2, respectively. (d) Absolute changes in ABDA absorbance at 402 nm as a function of the irradiation time.

For the Au–BSA NCs, the spectra in Fig. 4 also reveal weak photooxidation (Fig. 4b, inset), indicating that the photooxidation ability of these NCs is weak. This fact has already been noted in the literature for Au–BSA,[21] Au–GSH,[69] and Au-lysozyme[51] NCs. The PD activity of the fabricated Au–BSA–IgG–PS complexes is comparable to or even a bit higher than that observed for the free PS solution with an equivalent PS concentration. This enhanced PD activity of the Au–BSA–IgG–PS complexes could be due to possible synergistic addition of the PD activities of PS and Au-BSA NCs or simply to the minor difference between the PS concentrations in the free PS solution and in the Au–BSA–IgG–PS complexes.

2.2. Fluorescent Imaging of MSSA and MRSA

We first used the Au–BSA NCs and Au–BSA–IgG complexes as affinity probes for MSSA and MRSA. **Figure 5A** shows the control solutions of Au–BSA–IgG (1), Au–BSA (2), and PBS (3) in which *E. coli* (B, C), MSSA (D, E), and MRSA (F, G) were incubated. Intense red FL is observed for both Au–BSA–IgG and Au–BSA NCs. With the control PBS solution, none of the test tubes shows FL either before or after centrifugation and washing. After incubation of all three bacteria in Au–BSA–IgG and Au–BSA NC solutions, but before centrifugation and washing, the red FL color in all test tubes, marked by numbers 1 and 2, remains practically the same as shown in Fig. 5A. After centrifugation and washing of *E. coli*-containing test tubes C1 and C2, the NCs do not bind specifically to the bacteria and the sediment shows no red FL. Similarly, there is no FL for the sediments obtained with MSSA and MRSA after incubation with Au–BSA clusters, which do not contain targeting IgG molecules. In contrast, for MSSA and MRSA, the sediments clearly reveal red FL when the biospecific probe Au–BSA–IgG is used (tubes E1 and G1). Thus, these experiments give strong evidence for biospecific binding of Au–BSA–IgG complexes to MSSA and MRSA.

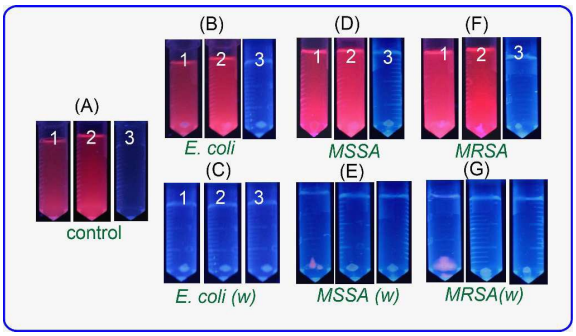

Figure 5. Photos obtained after incubation of *E. coli* (B, C), MSSA (D, E), and MRSA (F, G) in Au–BSA–IgG (1), Au–BSA (2), and PBS (3) solutions. Photos (A) show control solutions. Images B, D, and F were obtained after incubation and centrifugation and before washing in PBS. Images C, E, and G were obtained after the same treatment but after washing. For all samples, pH = 7.4.

An important comment is in order here. Recently, Chan and Chen[52] reported on the biospecific binding of *S. aureus* to Au–HSA FL NCs under acidic conditions (pH < 4–5). To compare this finding with the specificity of our IgG-containing complexes and to verify the possible nonspecific binding of NCs to *S. aureus* at low pH, we performed the following experiments. *E. coli*, MSSA, and MRSA were incubated in Au–BSA, Au–HAS, and PBS solutions (**Figure S7**, ESI) at pH 6 and 4. After centrifugation and washing at pH 6, no binding was observed in all nine experimental combinations (three different bacteria and three different incubation solutions). In contrast, at pH 4, we observed red FL sediments for both MSSA and MRSA incubated with either Au–BSA or Au–HSA complexes. Therefore, these observations confirm our assumption as to the nonspecific electrostatic binding of the albumins to the bacterial surface at acidic pH below the isoelectric point.

For evaluating the ability of the multifunctional Au–BSA NCs to selectively detect separate microbial cells or a group of cells, samples of *E. coli*, MRSA, and a mixture of both were examined by FL microscopy. Specifically, we investigated bacterial samples after incubation with Au–BSA–IgG complexes by using common transmission bright field (TBF) images and FL images under green and UV light illumination (**Figure 6**).

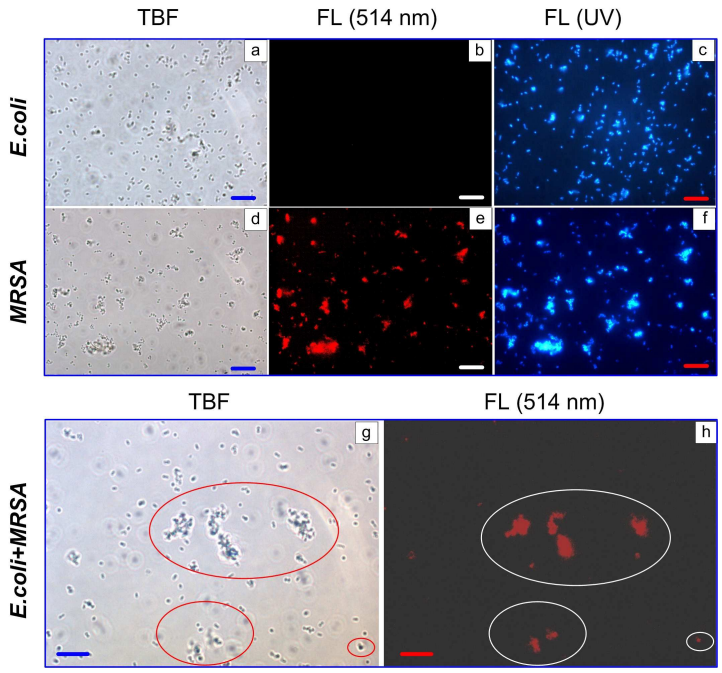

Figure 6. TBF (a, d, g) and FL images of *E. coli* (a, b, c), MRSA (d, e, f), and a mixture (g, h) of both bacteria under green light (514 nm) (b, e, h) and UV illumination (c, f). All samples were incubated in Au–BSA–IgG (PBS, pH 7.4) and were used for analysis after centrifugation and washing. The red and white ellipses show MRSA in the mixture. Bars are 10 μm.

The standard transmission images of both bacteria do not differ at a typical moderate magnification of about ×600, Fig. 6a and d). The only peculiarity is a certain tendency toward aggregation. Under UV illumination, both bacteria look similar and intense blue auto-FL is seen (Fig. 6c and f). However, under green light illumination, intense red FL can be observed only for target MRSA, whereas the *E. coli* control reveals no red FL. Evidently, we observe here the biospecific binding of the Au–BSA–IgG complexes to MRSA and the red FL is due to the Au–BSA NCs. Furthermore, the prepared Au–BSA–IgG complexes allow specific detection of target pathogenic bacteria in a mixture with nonspecific *E. coli*. Indeed, Fig. 6g shows a standard TBF image of *E. coli*–MRSA, in which the MRSA in red ellipses cannot be differentiated from *E. coli*. However, under green light illumination (Fig. 6h), the intense red FL clearly indicates the presence of pathogenic MRSA (white ellipses).

2.3. PD Inactivation of Microorganisms

PD inactivation of MSSA and MRSA was performed as described in Experimental Section. Several controls were made to elucidate the specific role of PS in PD inactivation under treatment with laser light and incubation in different PD agents. PBS, Au–BSA, and Au–BSA–IgG complexes were used as negative controls. Note, however, that Au–BSA complexes themselves (with no PD dye added) have a weak PD activity. The positive controls were a free PS solution and Au–BSA–PS complexes. The most effective PD inactivation was expected from complete Au–BSA–IgG–PS complexes.

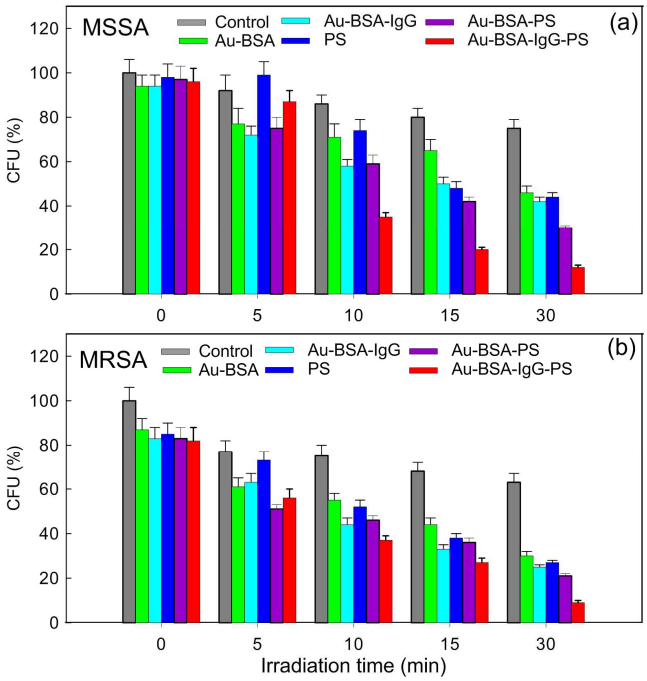

Figure 7. Viability of MSSA (a) and MRSA (b) as a function of the irradiation time (wavelength, 660 nm; power density, 25 mW/cm^2) after incubation with PS, Au–BSA NCs, and Au–BSA–IgG, Au–BSA–PS, and Au–BSA–IgG–PS complexes. Before PD treatment, the bacteria were incubated in the dark for 15 min in the appropriate solutions. The maximal delivered fluence was 45 J/cm^2.

It follows from **Figure 7** that all solutions exhibited low dark toxicity to MSSA and somewhat higher dark toxicity to MRSA. Incubation with different solutions for 15 min suppressed the number of CFU to 97% and 85% of the total number, respectively. A quite unexpected result is the noticeable death of cells (survivability, ca. 75% and 63%) irradiated for 30 min in the absence of photodynamic agents (PBS control). The antimicrobial PD activity of the different solutions depended strongly on the irradiation time. For example, under short-time exposure (less than 5 min), the PD activity decreased in the order PBS< PS< Au–BSA~Au–BSA–IgG<Au–BSA–PS<Au–BSA–IgG–PS. Under a 30-min exposure, the PD inactivation of MRSA was more effective compared to that of MSSA; the strongest inactivation (about 90%) was observed for complete Au–BSA–IgG–PS complexes. Surprisingly enough, the antimicrobial activity of free PS was almost comparable to that of the different types of NCs and complexes that did not include PS in their composition. The basic mechanism behind the lethal PD damage to bacteria is associated with possible damage to the cytoplasmic membrane, whereas

DNA destruction is believed to play only a supplementary role.[70,71] Thus, the observed effective inactivation of MRSA can be explained by the biospecific targeting through IgG molecules and by the synergistic PD action of PS and Au–BSA NCs.

It is of interest to compare the efficacy of our PD treatment with photothermal (PT) treatments in terms of the delivered fluence. In our case, the power density was 25 mW/cm^2, the irradiation time varied from 5 to 30 min, and the delivered fluence increased from 7.5 to 45 J/cm^2. Maximal MSSA and MRSA cell death was about 90% for both bacteria. Recently, Millenbaugh et al.[31] reported PT inactivation of MSSA and MRSA with 40-nm gold nanoparticles conjugated with targeting antibodies. Under plasmon resonance irradiation at 532 nm and at a delivered fluence of 500 J/cm^2 (100 pulses of 5 J/cm^2 each), the killing efficiency was 69% and 42% for MSSA and MRSA, respectively. A similar model was studied by Zharov et al.,[48] who showed that at a laser pulse fluence of 0.5–1 J/cm^2, at least 100 pulses are required to produce harmful effects on *S. aureus*. Tuchina *et al*.[50] achieved 95% PT killing with targeted Au nanorods, plasmonic irradiation at CW 808 nm, and a fluence of 180 J/cm^2. Thus, the developed Au–BSA–IgG–FS complexes demonstrate high PD efficiency at a minimal delivered fluence for the inactivation of *S. aureus*.

3. Conclusion

We have developed novel Au–BSA–antiSAIgG–PS complexes to achieve selective targeting toward the pathogenic bacteria MSSA and MRSA and the delivery of the Photosens^{TM} PS for PD therapy. The developed nanoplatform exhibited three theranostic modalities: biospecific detection due to antiSAIgG targeting, intense red FL due to Au–BSA NCs with a QY of about 14%, and synergistic PD inactivation due to the photosensitizer Photosens^{TM}. PD treatment of MSSA and MRSA with Au–BSA–antiSAIgG–PS complexes and 660-nm light irradiation effectively kills both types of bacteria. In contrast to the biospecific binding of Au–BSA–antiSAIgG to MSSA and MRSA at physiological pH of 7.4, the binding of the Au–HSA and Au–BSA NCs to MSSA and MRSA at pH < 6 (Chan and Chen, *Anal. Chem*, **2012**, *84*, 8952) seems nonspecific because of the purely electrostatic binding mechanism. The developed complexes can be further modified by changing the photosensitizer (including the use of natural photosensitizers[72]), tailoring the targeting molecules, and loading with effective drugs. Such modifications would ensure new theranostic applications in current nanomedicine.

4. Experimental Section

Materials: 1-ethyl-3-[3-dimethylaminopropyl]carbodiimide hydrochloride (EDC), N-hydroxysuccinimide (NHS), 10-anthracenediyl-bis (methylene) dimalonic acid (ABDA), hydrogen tetrachloroaurate(III) hydrate ($HAuCl_4$), bovine serum albumin (BSA), and human serum albumin (HSA) were all obtained from Sigma–Aldrich. The photosensitizer Photosens^{TM} (0.2% water solution of aluminium phthalocyanine, PS) was obtained from the Institute of Organic Intermediates and Dyes (Moscow, Russia). Human antistaphylococcal immunoglobulins (antiSA-IgG; here designated IgG for brevity) were from Microgen (Russia).

Synthesis of Au NCs and multifunctional complexes: First, Au–BSA NCs were prepared by protein-directed synthesis at high temperature and pH.[54] In a typical synthesis, 5 mL of 11.6 mM $HAuCl_4$ was added to 5 mL of a BSA solution (38.4 mg/mL) under vigorous magnetic stirring for 2 min. Then, 380 mL of 1M NaOH was added. This mixture was heated in an oil bath at 100 °C for 1 h under vigorous magnetic stirring. During this period, the solution color changed from light-yellow to brown, indicating the formation of small Au NCs. After the solution had been cooled to room temperature, the product was collected with an Amicon Ultra-15 centrifuge concentrator (MW cutoff, 10000) and was redispersed in 19 mL of 10 mM PBS (pH 7.4). The final BSA concentration was 10 mg/mL.

Au–HSA NCs were prepared by a similar procedure but with modified reagent concentrations (ESI, section S1).

Au–BSA NCs were conjugated with antiSA-IgG by using EDC and NHS as zero-length crosslinkers.[66] Five mL of Au–BSA NCs (10 mg/mL) was mixed with 5 mL of antiSA-IgG (2 mg/mL) in 10 mM PBS. Then, EDC and NHS were added to final concentrations of 50 and 5 mM, respectively.[73] The mixture was incubated at room temperature for 2 h. The Au–BSA–IgG complexes were purified by gel filtration on a PD-10 desalting column.

Since the plasma protein binding of PS is about 97%,[74] PS was loaded into Au–BSA–IgG by simple mixing of the conjugate with PS. Briefly, 200 μL of 0.2% PS was added to 10 mL of Au–BSA–IgG (BSA concentration, 10 mg/mL) and the mixture was incubated at room temperature for 1 h. After that, the product was desalted and purified on a PD-10 column, yielding Au–BSA–IgG–PS multifunctional complexes.

Successful conjugation of IgG with Au–BSA was confirmed by testing the biospecific interaction of antiSA-IgG with protein A and MRSA with a dot immunoassay (Fig. S4, ESI). Successful loading of PS into the final product was confirmed by UV–vis and FL spectroscopy. Au–BSA–PS complexes were obtained by the same procedure but with Au–BSA as a nanocarrier.

Characterization: FL spectra were recorded with an LS-55 FL spectrophotometer (Perkin Elmer). Absorption spectra were recorded with a Specord 250BU UV–vis spectrophotometer (Analytik Jena, Germany). TEM images were taken with a Libra-120 microscope (Carl Zeiss) at the Simbioz Center for the Collective Use of Research Equipment in the Field of Physical–Chemical Biology and Nanobiotechnology at the IBPPM RAS. Images of the samples under UV irradiation were captured with a Canon digital camera and a Vilber Lourmart transilluminator (365 nm, Sigma–Aldrich). Transmitted light BF images and FL images of bacteria under 405-nm and 514-nm excitation were recorded with a Leica DM 2500 microscope equipped with a 100× immersion objective.

Generation of singlet oxygen was detected spectrophotometrically with a singlet oxygen sensor, 9,10-anthracenediyl-bis (methylene) dimalonic acid (ABDA) [68]. Solutions of Au–BSA, Au–BSA–IgG–PS, and free PS were prepared in 10 mM PBS and were adjusted to equal concentrations of PS (200 ng/mL); 25 μL of 2 mg/mL ABDA was then added to 2.5 mL of the solutions being tested, separately. The mixtures were irradiated with a LED light source for medical PD therapy (660 nm, 300 mW, Russia) at a power density of 50 mW/cm^2. The generation of singlet oxygen was detected by recording the decrease in ABDA absorption at 407 nm after different light exposures.

Misroorganisms: Methicillin-sensitive *S. aureus* 209 P (MSSA), methicillin-resistant *S. aureus* (MRSA), and *Escherichia coli* were obtained from Tarasevich State Science Research Institute for the Standartization and Control of Medical Biological Preparations, Moscow. Bacteria were grown on an all-purpose solid nutrient medium (GRM agar, Obolensk, Russia) at 37°C. The bacterial concentration was determined from absorbance data. In FL imaging experiments, bacteria grown on solid nutrient medium at 37°C for 24 h were suspended in sterile 10 mM PBS and were adjusted to the absorbance $A_{600} = 0.9$ in a 1-cm cuvette. The pH dependence of NS probe binding to bacteria was examined by adjusting the pH of PBS to 4 and 6.

In PD experiments, the grown cells of MSSA and MRSA (37 °C, 24 h) were suspended in sterile 10 mM PBS and the cell concentration was adjusted by sequential tenfold dilutions to 10^3 microbial cells/mL.

FL imaging experiments: For bacterial sensing experiments, the fabricated Au–BSA, Au–HSA, and Au–BSA–IgG NCs (50 μL; albumin concentration, 2 mg/ mL) were added to a bacterial solution (1.8 mL; absorbance *A*600, 0.9) at an appropriate pH (7.4, 6, or 4) and then were vortex mixed for 2 h. After centrifugation at 6500 rpm for 5 min, the resulting solution was examined under UV light ($\lambda_{max} = 365$ nm).

For FL microscopy imaging, the treated bacteria were fixed by adding formaldehyde (final concentration, 0.1%). Ten μL of MRSA, *E. coli*, or a mixture of both was placed between microscopic glasses, and images were acquired in the phase contrast (white light) and FL (UV excitation and excitation at 514 nm) modes.

Photodynamic experiments: For irradiation of samples, an LED light source (660 nm, 300 mW; power density, 25 mW/cm^2) was used. All experiments were conducted in the CW irradiation mode. For generating aseptic conditions, we used sterile disposable polystyrene 96-well plates. All photosensitizer solutions were sterilized by filtration through 0.2-μM styrene filters. The light sources were placed above the plate wells.

The PD sensitizers were five types of solutions, including a PS solution in PBS; Au–BSA NCs; and Au–BSA–PS, Au–BSA–IgG, and Au–BSA–IgG–PS complexes. For all solutions, the final concentration of PS was 2 mg/L and the BSA concentration was 1 g/L.

In a typical experiment, 0.1 mL of a PD agent solution was added to 0.9 mL of a bacterial culture (cell concentration, 10^3 cells/mL) and the mixture was incubated for 15 min in the dark. From each incubated mixture, 0.1 mL was placed in a plate well and was exposed to LED light (660 nm) for 5, 10, 15, and 30 min. Next, the bacterial suspensions were transferred from the wells to petri dishes containing solid nutrient medium and were uniformly distributed over the surface with a sterile spreading rod. The results were estimated by counting the number of colony-forming units (CFU) at 24 h after incubation at 37°C. Bacterial suspensions that were not irradiated or PD treated served as controls. All experiments were run in triplicate.

Acknowledgements

Work by BK and NK on the synthesis and characterization of NCs and the complexes was supported by the Russian Scientific Foundation (project no. 14-13-01167). The work by VT on the PD inactivation of bacteria was supported by the Russian Scientific Foundation (project no. 14-15-00186). TEM analysis was partly supported by grant no. 14.Z50.31.0004 to support scientific research projects implemented under the supervision of leading scientists. We thank Leonid Dolotov for his help with power density measurements and Maria Karchenova for her help with PD inactivation studies. We also thank Mr. D.N. Tychinin (IBPPM RAS) for his help in preparation of the manuscript.

The table of contents entry:

A novel fluorescent nanocluster platform is developed that combines three theranostic modalities. Specfically, Au–BSA–antiSAIgG–PS complexes exhibit intense red fluorescence due to Au_{25}–BSA nanoclusters with a quantum yield of about 14%, biospecific binding to *S. aureus* due to human antistaphylococcal immunoglobulin (antiSAIgG), and synergistic photodynamic inactivation due to the photosensitizer Photosens™ (PS).

Keyword: fluorescent Au nanoclusters, functionalized nanoclusters, Photosens™, photodynamic therapy, pathogenic bacteria

Multifunctional Au nanoclusters for targeted bioimaging and enhanced photodynamic inactivation of *Staphylococcus aureus*

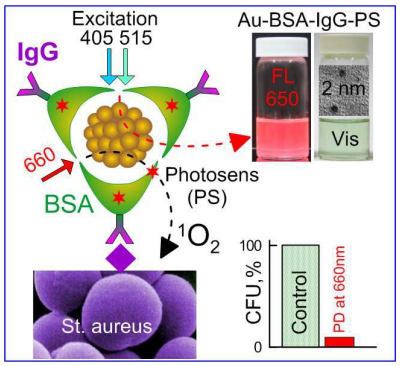

RSC Advances

ARTICLE

Notes and references

1 J. Zheng and R. M. Dickson, *J. Am. Chem. Soc*., 2002, **124**, 13982.
2 J. Zheng, J. T. Petty and R. M. Dickson, *J. Am. Chem. Soc*., 2003, **125**, 7780.
3 J. Zheng, C. Zhang and R. M. Dickson, *Phys. Rev. Lett.*, 2004, **93**, 077402.
4 L. Shang, S. Dong and G.U. Nienhaus, *Nano Today*, 2011, **6**, 401.
5 S. Choi, R. M. Dickson and J. Yu, *Chem. Soc. Rev.*, 2012, **41**, 1867.
6 Y. Lu and W. Chen, *Chem. Soc. Rev*., 2012, **41**, 3594.
7 L. Zhang and E. Wang, *Nano Today*, 2014, **9**, 132.
8 Y. Negishi, K. Nobusada and T. Tsukuda, *J. Am. Chem. Soc*., 2005, **127**, 5261.
9 P. Zhang, *J. Phys. Chem. C*, 2014, **118**, 25291.
10 R. Jin, *Nanoscale*, 2015, **7**, 1549.
11 P. Yu , X. Wen, Y.-R. Toh, X. Ma and J. Tang, *Part. Part. Syst. Charact*., 2015, **32**, 142.
12 T. Huang and R. W. Murray, *J. Phys. Chem. B*, 2001, **105**, 12498.
13 J. Liu, *Trends Anal. Chem*., 2014, **58**, 99.
14 Y. Yu, Q.Yao, Z. Luo, X. Yuan, J. Y. Lee, J. Xie, *Nanoscale*, 2013, **5**, 4606.
15 A. Mathew and T. Pradeep, *Part. Part. Syst. Charact*., 2014, **31**, 1017.
16 J. Xie, Y. Zheng and J. Y. Ying, *J. Am. Chem. Soc*., 2009, **131**, 888.
17 D. M. Chevrier, A. Chatt and P. Zhang, *J. Nanophotonics*, 2012, **6**, No. 064504.
18 Y. Xu, J. Sherwood, Y. Qin, D. Crowley, M. Bonizzoni and Y. Bao, *Nanoscale*, 2014, **6**, 1515.
19 J. Wang, G. Zhang, Q. Li, H. Jiang, C. Liu, C. Amatore and X. Wang, *Sci. Rep*., 2013, **3**, 1157.
20 J. Wang, J. Ye, H. Jiang, S. Gao, W. Ge, Y. Chen, C. Liu, C. Amatore and X. Wang, *RSC Adv*., 2014, **4**, 37790.
21 X.-D. Zhang, D. Wu, X. Shen, P.-X. Liu, F.-Y. Fan and S.-J. Fan, *Biomaterials*, 2012, **33**, 4628.
22 Wu, X. He, K. Wang, C. Xie, B. Zhou and Z. Qing, *Nanoscale*, 2010, **2**, 2244.
23 H. Chen, B. Li, C. Wang, X. Zhang, Z. Cheng, X. Dai, R. Zhu and Y. Gu, *Nanotechnology*, 2013, **24**, 055704.
24 K. Selvaprakash and Y.-C. Chen, *Biosens. Bioelectron*., 2014, **61**, 88.
25 L.-Y. Chen, C.-W. Wang, Z. Yuan and H.-T. Chang, *Anal. Chem*., 2015, **87**, 216.
26 G. Li and R. Jin, *Acc. Chem. Res*., 2013, **46**, 1749.
27 G. Korotcenkov, V. Brinzari and B. K. Cho, *Mater. Lett*., 2015, **147**, 101.
28 M. P. Jevons, A. W. Coe and M. T. Parker, *Lancet*, 1963, **1**, 904.
29 R. H. Deurenberg, C. Vink, S. Kalenic, A. W. Friedrich and C. A. Bruggeman, *Clin. Microbiol. Infec*., 2007, **13**, 222.
30 D. Carnicer-Pont, K. A. Bailey, B. W. Mason, A. M. Walker, M. R. Evans and R. L. Salmon, *Epidemiol. Infect*., 2006, **134**, 1167.
31 N. J. Millenbaugh, J. B. Baskin, M. N. DeSilva, W. R. Elliott and R. D. Glickman, *Int. J. Nanomedicine*, 2015, **10**, 1953.
32 X. Dai, Z. Fan, Y. Lu and P. C. Ray, *ACS Appl. Mater. Interfaces*, 2013, **5**, 11348.
33 F. J. Picard and M. G. Bergeron, *Drug. Discov. Today*, 2002, **7**, 1092.
34 J. Funkhouser, *Curr. Drug. Discov*., 2002, **2**, 17.
35 S. Warner; T. Lammers, S. Aime, W. E. Hennink, G. Storm and F. Kiessling, *Acc. Chem. Res*., 2011, **44**, 1029.
36 S. S. Kelkar and T. M. Reineke, *Bioconjug. Chem*., 2011, **22**, 1879.
37 N. Khlebtsov, V. Bogatyrev, L. Dykman, B. Khlebtsov, S. Staroverov, A. Shirokov, L. Matora, V. Khanadeev, T. Pylaev, N. Tsyganova and G. Terentyuk, *Theranostics*, 2013, **3**, 167; *Erratum*: 2013, **3**, 1012.
38 L. Dong, M. Li, S. Zhang, J. Li, G. Shen, Y. Tu, J. Zhu and J. Tao, *Small*, 2015, **11**, 2571.
39 N. G. Khlebtsov and L. A. Dykman, *Chem. Soc. Rev.*, 2010, **40**, 1647.

40 R. Bardhan, S. Lal, A. Joshi and N. J. Halas, *Acc. Chem. Res*., 2011, **44**, 936.
41 R. M. Cabral and P. V. Baptista, *Expert Rev. Mol. Diagn*., 2014, **14**, 1041.
42 A. Retnakumari, S. Setua, D. Menon, P. Ravindran, H. Muhammed, T. Pradeep, S. Nair and M. Koyakutty, *Nanotechnology,* 2010, **21**, 55103.
43 Y. Wang, J. Chen and J. Irudayaraj, *ACS Nano*, 2011, **5**, 9718.
44 H. Chen, S. Li, B. Li, X. Ren, S. Li, D. M. Mahounga, S. Cui, Y. Gu and S. Achilefu, *Nanoscale*, 2012, **4**, 6050.
45 H. Chen, B. Li, X. Ren, S. Li, Y. Ma, S. Cui, and Y. Gu, *Biomaterials*, 2012, **33**, 8461.
46 C. Ding and Y.Tian, *Biosens. Bioelectron*., 2015, **65**, 183.
47 C. Zhang, C. Li, Y. Liu, J. Zhang, C. Bao, S. Liang, Q. Wang, Y. Yang, H. Fu, K. Wang and D. Cui, *Adv. Func. Mater*., 2015, **25**, 1314.
48 V. P. Zharov, K. E. Mercer, E. N. Galitovskaya and M. S. Smeltzer, *Biophys. J*., 2006, **90**, 619.
49 B. N. Khlebtsov, E. S. Tuchina, V. A. Khanadeev, E. V. Panfilova, P. O. Petrov, V. V. Tuchin and N. G. Khlebtsov, *J. Biophotonics*, 2013, **6**, 338.
50 E. S. Tuchina, P. O. Petrov, K. V. Kozina, F. Ratto, S. Centi, R. Pini and V. V. Tuchin, *Quant. Electron*., 2014, **44**, 683.
51 W.-Y. Chen, J.-Y. Lin, W.-J. Chen, L. Luo, E. W.-G. Diau and Y.-C. Chen, *Nanomedicine*, 2010, **5**, 755.
52 P.-H. Chan and Y.-C. Chen, *Anal. Chem*., 2012, **84**, 8952.
53 L. B. Josefsen and R. W. Boyle, *Theranostics*, 2012, **2**, 916.
54 P. Zhang, X. X. Yang, Y. Wang, N. W. Zhao, Z. H. Xiong and C. Z. Huang, *Nanoscale*, 2014, **6**, 2261.
55 X. Wen, P. Yu, Y.-R. Toh and J. Tang, *J. Phys. Chem. C*, 2012, **116**, 11830.
56 D. G. Duff, A. Baiker, *Langmuir*, 1993, **9**, 2301.
57 A. K. Sahoo, S. Banerjee, S. S. Ghosh and A. Chattopadhyay. *ACS Appl. Mater. Interfaces*, 2014, **6**, 712.
58 Z. Wu, J. Chen and R. Jin, *Adv. Funct. Mater*. 2011, **21**, 177.
59 Y. Yu, Z. Luo, D. M. Chevrier, D. T. Leong, P. Zhang, D. Jiang, J. Xie, *J. Am. Chem. Soc*., 2014, **136**, 1246.
60 Z. Luo, X. Yuan, Y. Yu, Q. Zhang, D. T. Leong, J. Y. Lee, and J. Xie, *J. Am. Chem. Soc*., 2012, **134**, 16662.
61 G. Cauzzo, C. Gennari, G. Jori and J. D. Spikes, *Photochem. Photobiol*., 1977, **25**, 389.
62 D. F. Eaton, *J. Photochem. Photobiol. B*, 1988, **2**, 523.
63 J. R. Lakowicz, Principles of Fluorescence Spectroscopy. 3-rd ed., Springer, New York 2006.
64 S. Link, A. Beeby, S. FitzGerald, M. A. El-Sayed, T. G. Schaaff and R. L. Whetten, *J. Phys. Chem. B*, 2002, **106**, 3410.
65 J. Zheng, P. R. Nicovich and R. M. Dickson, *Annu. Rev. Phys. Chem*., 2007, **58**, 409.
66 G. T. Hermanson. Bioconjugate Techniques, Academic Press, San Diego, New York, Boston, 1996.
67 B. Khlebtsov and N. Khlebtsov, *Nanotechnology*, 2008, **19**, 435703.
68 A. A. Stratonnikov, N. V. Ermishova, G. A. Meerovich, B. V. Kudashev, E. G. Vakulovskaya and V. B. Loschenov, *Proc. SPIE*, 2002, **4613**, 162.
69 Y.-S. Chen and P. V. Kamat, *J. Am. Chem. Soc*., 2014, **136**, 6075.
70 M. R. Hamblin and T. Hasan, *Photochem. Photobiol. Sci*., 2004, **3**, 436.
71 B. C. Wilson, in: Handbook of Photonics for Biomedical Science, V. V. Tuchin (ed.), CRC Press, Taylor & Francis, London, 2010, p. 649.
72 P. Neelakantan, C. Q. Chenga, V. Ravichandran, T. Mao, P. Sriraman, S. Sridharan, C. Subbarao, S. Sharma and A. Kishen, *Photodiagn. Photodyn*., 2014, **12**, 108.
73 H. Liu, X. Wu, X. Zhang, C. Burda and J.-J. Zhu, *J. Phys. Chem. C*, 2012, **116**, 2548.
74 V. V. Tuchin (Ed.), Advanced Optical Flow Cytometry: Methods and Disease Diagnoses, Wiley-VCH Verlag GmbH & Co. KGaA, Weinheim, Germany, 2011.